



Cite this: *Phys. Chem. Chem. Phys.*,  
2024, 26, 9534

# Microstrain effects of laser-ablated Au nanoparticles in enhancing CZTS-based 1 Sun photodetector devices†

Serap Yiğit Gezgin,<sup>a</sup> Walid Belaid,<sup>ib</sup> <sup>a</sup> Mohamed A. Basyooni-M. Kabatas,<sup>ib</sup> \*<sup>bcd</sup>  
 Yasin Ramazan Eker<sup>de</sup> and Hamdi Şükür Kilic<sup>ib</sup> <sup>afg</sup>

Copper zinc tin sulfide (CZTS) thin films were synthesized on soda lime glass using pulsed laser deposition (PLD) at room temperature. Introducing gold nanoparticles (AuNPs) in a sandwich structure led to increased CZTS particle size and a shift in the localized surface plasmon resonance (LSPR) peak of the AuNPs, influenced by different laser energy levels. The absorption measurements revealed intriguing behavior across the visible and near-infrared (NIR) regions, making these films appealing for 1 Sun photodetectors. Furthermore, the presence of AuNPs in the sandwich structure reduced microstrain effects, measuring  $1.94 \times 10^{-3}$  compared to  $3.38 \times 10^{-3}$  in their absence. This reduction directly enhances carrier transport, which is particularly beneficial for accelerating the performance of photodetector devices. This effect of AuNPs also contributed to higher dielectric coefficients, further improving the photodetector performance. Under 1 Sun illumination conditions, this enhancement resulted in a rapid rising time of 95.4 ms, showcasing the potential for faster photodetection.

Received 18th January 2024,  
Accepted 26th February 2024

DOI: 10.1039/d4cp00238e

rs.c.li/pccp

## 1. Introduction

CZTS material, which is used as an active and absorber layer in solar cells, has a distinctive feature of a high absorption coefficient ( $>10^4 \text{ cm}^{-1}$ ) in the visible region and consists of low-cost and non-toxic elements.<sup>1–3</sup> The high-absorbing CZTS material could be used in photodetectors and solar cell applications. Photodetectors are pivotal in diverse fields, encompassing communications, imaging, and environmental sensing. Nevertheless, prevailing challenges such as response speed, sensitivity, and fabrication cost necessitate continuous

advancement in photodetector materials. In this context, CZTS thin films offer an intriguing avenue for exploration, leveraging their unique properties to address these challenges.<sup>4,5</sup>

Light trapping methods increase the absorbency of thin films produced at very low thicknesses. Among these methods, plasmonic nanoparticles (NPs) can be composed of Au, Cu, and Ag metals. These plasmonic NPs exhibit remarkable optical properties like localized surface plasmon resonance (LSPR).<sup>6,7</sup> LSPR is a phenomenon where the electromagnetic field (EMF) of the light incident on the plasmonic NP stimulates the electrons in the particle, causing them to move simultaneously.<sup>8</sup> The wavelength at which the LSPR peak appears varies with the particle size, shape, density, and environment. The technique used in producing the particle is essential in changing the morphological structure of plasmonic NPs. Particle growth can be achieved close to the desired density, size, and shape by quickly adjusting the parameters of the PLD<sup>9,10</sup> experimental system, such as laser pulse number,<sup>11,12</sup> laser energy, laser wavelength, and substrate temperature.<sup>13–15</sup> A PLD system mainly consists of a laser system and a vacuum chamber. Thus, the morphological, optical, crystalline, and electrical properties of thin films produced by PLD can be easily adjusted.<sup>16–19</sup>

This study produced CZTS thin films in 61 nm and 112 nm thickness using the PLD technique, depending on the number of laser pulses. Au plasmonic NPs were grown on soda lime glass (SLG) depending on laser energy per pulse, and AuNPs@CZTS thin films were produced by embedding Au nanoparticles into

<sup>a</sup> Department of Physics, Faculty of Science, Selçuk University, Konya, 42075, Turkey

<sup>b</sup> Dynamics of Micro and Nano Systems Group, Department of Precision and Microsystems Engineering, Delft University of Technology, Mekelweg 2, 2628 CD Delft, The Netherlands. E-mail: M.kabatas@tudelft.nl  
 Web: <https://m.a.basyooni@gmail.com>

<sup>c</sup> Solar Research Laboratory, Solar and Space Research Department, National Research Institute of Astronomy and Geophysics, 11421 Cairo, Egypt

<sup>d</sup> Science and Technology Research and Application Center (BITAM), Necmettin Erbakan University, 42090 Konya, Turkey

<sup>e</sup> Department of Basic Sciences, Faculty of Engineering, Necmettin Erbakan University, 42090 Konya, Turkey

<sup>f</sup> Directorate of High Technology Research and Application Center, University of Selçuk, 42031 Konya, Turkey

<sup>g</sup> Directorate of Laser-Induced Proton Therapy Application and Research Center, University of Selçuk, 42031 Konya, Turkey

† Electronic supplementary information (ESI) available. See DOI: <https://doi.org/10.1039/d4cp00238e>



CZTS thin films with the highest laser energy. Optical, morphological, crystalline, and electrical properties, including the photo-sensing properties of CZTS and AuNPs@CZTS thin films, were investigated in detail. In the subsequent sections, we present the growth technique employed, the discerned outcomes, an in-depth analysis, and the overarching implications of our findings. This endeavor not only furthers our understanding of photodetector materials but also underscores the potential of CZTS thin films and plasmonic NPs in shaping the future of optoelectronic devices.

## 2. Fabrication and characterization

A Continuum Minilite II pulsed laser device operating at 1064 nm wavelength, five ns pulse width, and 10 Hz repetition rate was used to deposit CZTS and AuNPs@CZTS thin films. The target–substrate distance in the vacuum chamber was set at 45 mm, and the atmosphere inside the vacuum chamber was evacuated down to  $10^{-6}$  mbar background pressure to form a clean environment for deposition. First, the Au sputtering target (99.95%) was ablated by a laser beam with 36 mJ, 32 mJ, 30 mJ, and 26 mJ energies per pulse, and its NP thin film was deposited on the SLG substrate at room temperature.

Second, the CZTS sputtering target, with a purity of 99.99%, underwent ablation by a laser beam set at a pulse energy of 15 mJ. The process utilized 2400 pulses to deposit CZTS(1) thin films with a thickness of 61 nm and 4800 pulses for CZTS(2) thin films measuring 112 nm in thickness, both on soda lime glass (SLG) substrates at ambient temperature. Au nanoparticles were ablated using 36 mJ laser pulse energies, which were embedded into these CZTS(1) and CZTS(2) thin films, and thus the plasmonic AuNPs@CZTS(1) & AuNPs@CZTS(2) thin films were produced. The sulfurization process involved subjecting the material to a quartz tube furnace under vacuum conditions, maintaining a temperature of 375 °C for 45 minutes. During this process, 50 mg of sulfur powder was placed adjacent to the material undergoing treatment. The final structure is schematically shown in Fig. 1.

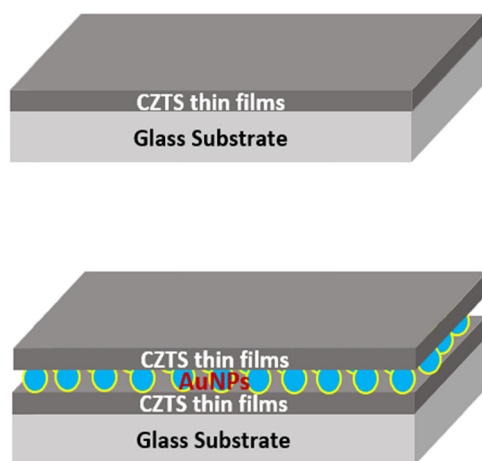


Fig. 1 Schematic design of CZTS and AuNPs@CZTS thin-film photodetectors.

### 2.1. Device characterization

The crystalline, optical, and morphological properties of CZTS and AuNPs@CZTS thin films were examined using several analytical techniques. Structural and phase parameters were analyzed using a Panalytical Empyrean instrument with  $\text{CuK}\alpha$  radiation through X-ray diffractometry. Surface morphology was investigated using a ZEISS GeminiSEM 500 scanning electron microscope (SEM). The optical absorption spectra were measured using a 200–2000 nm UV-Vis-NIR spectrophotometer. The electrical properties of the thin film samples were assessed through electrical current–voltage ( $I$ – $V$ ) and optoelectronic measurements using an OptoSense solar simulator connected to a source meter. The light source has an AM1.5G filter at 1 Sun of  $100 \text{ mW cm}^{-2}$  illumination.

## 3. Results and discussion

### 3.1. XRD analyses

CZTS(1) and CZTS(2) thin films of 61 nm and 112 nm thicknesses and AuNPs@CZTS(1) & (2) thin films are produced by embedding AuNPs into these thin films. All CZTS thin films present (112), (200), and (220) crystal orientations located at  $28^\circ$ ,  $33^\circ$ , and  $47^\circ$  ( $2\theta$ ) in the XRD pattern in Fig. 2a, respectively.<sup>1</sup> CZTS(1)-thin film indicates the weakest crystal structure. The crystal structure of CZTS(2)- thin film has been developed, and its central peak density is higher. As the number of laser pulses increased, the deposited atoms nucleated better on the substrate, filled the appropriate vacancies, and made better alignment in the crystal structure.<sup>1</sup> In AuNPs@CZTS thin films, (111) crystal-oriented peaks of the Au element also appeared on the  $2\theta = 38^\circ$  angle.<sup>20</sup> The number of Au atoms is excessive for the very thin CZTS(1) thin film, so that it can occupy undesirable places in the crystal structure. Thus, the central peak of AuNPs@CZTS(1) has been weakened. However, with the addition of AuNPs, the central peak density of the AuNPs@CZTS(2) thin film increases, and its crystal structure improves.<sup>20,21</sup>

Fig. 2b presents the Raman spectroscopic analysis of the CZTS1 thin film. The dominant peak at  $337 \text{ cm}^{-1}$  is indicative of the kesterite  $\text{Cu}_2\text{ZnSnS}_4$  phase.<sup>22–24</sup> Additionally, two secondary peaks at  $267 \text{ cm}^{-1}$  and  $290 \text{ cm}^{-1}$  are observed, corresponding to the  $\text{Cu}_2\text{SnS}_3$  (CTS) secondary phase.<sup>25,26</sup> The emergence of the CTS phase is likely due to the predominance of Sn over Zn despite a marginally reduced Cu content,<sup>27,28</sup> as quantified in Table 2.

The primary grain size of all CZTS thin films has been calculated *via* the Scherrer equation that is stated by eqn (1):<sup>1</sup>

$$D = 0.94\lambda/\beta \cos \theta \quad (1)$$

$D$  is the crystal size,  $\lambda$  is the wavelength of X-ray,  $\theta$  is the Bragg diffraction angle, and  $\beta$  is the full-width at half-maximum of diffraction of the central peak. Crystal sizes of CZTS(1), AuNPs@CZTS(1), CZTS(2), and AuNPs@CZTS(2) thin films have been determined to be 7.34 nm, 12.1 nm, 10.71 nm, and 18.64 nm, respectively. The crystal size expanded with increases in thin film thicknesses from CZTS(1) to CZTS(2). So, with some gains in the number of laser pulses, the deposition



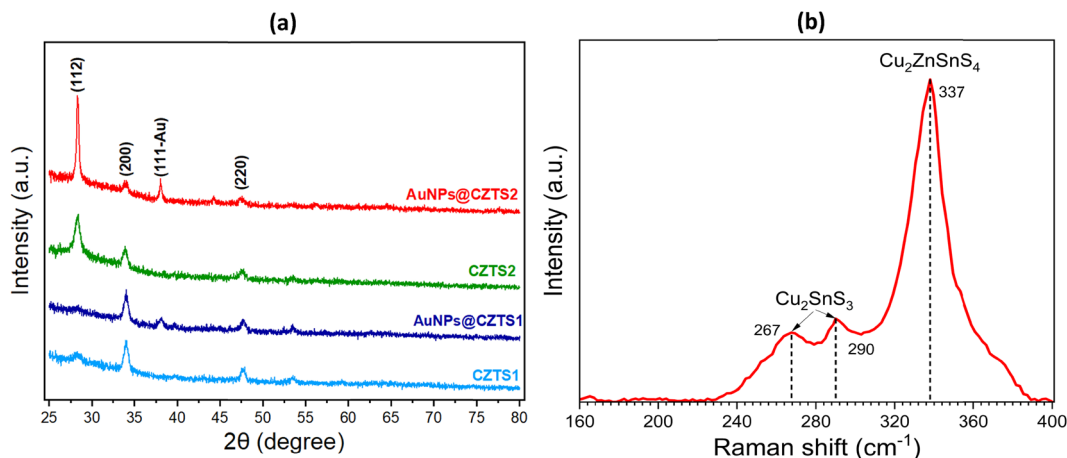


Fig. 2 (a) XRD spectrum of CZTS and AuNPs@CZTS thin films, (b) Raman spectrum of CZTS1 thin film.

rate increases, and thus, the grain size increases. Grain boundaries were decreased, and the traps and defects in these boundaries were passivated. Thus, the crystal structure of CZTS(2) has improved. The crystal size of AuNPs@CZTS thin films is more significant than that of non-Au embedded CZTS thin films.  $\text{Au}^{3+}$  ions can occupy  $\text{Zn}^{2+}$  vacancies. Since the  $\text{Au}^{3+}$  ionic radius (85 p.m.) is more comprehensive than the  $\text{Zn}^{2+}$  ionic radius (74 p.m.), it causes some increases in the crystal size of AuNPs@CZTS thin films.<sup>29,30</sup> However, since the density of AuNPs in AuNPs@CZTS(1) was excessive compared to the thickness of CZTS(1) thin film, and the intensity of the prominent peak in the (112) direction that is weakened by occupying the unsuitable voids in the crystal structure.<sup>31–33</sup> Since the thin film of CZTS(2) was thicker, the density of AuNPs did not adversely affect its crystal structure; on the contrary, the density of the main peak was enhanced.

The dislocation density ( $\delta$ ) and microstrain ( $\varepsilon$ ) expressed by eqn (2) and (3) cause the formation of defect structures in the thin films and the deterioration of their crystal structure.

$$\delta = \frac{1}{D^2} \quad (2)$$

$$\varepsilon = \frac{\beta \cos \theta}{4} \quad (3)$$

As presented in Table 1, since CZTS(1) has a smaller grain size, there are many defects and traps within the grain boundary numbers, and  $\delta$  and  $\varepsilon$  are high. The grain size of AuNP@CZTS(2) is wider than the other thin films,  $\delta$  and  $\varepsilon$  reduced because the grain boundary numbers are decreased. Furthermore, since plasmonic NPs enhance grain size, the dislocation density and

microstrain of CZTS thin films are diminished.<sup>16</sup> The measurement of microstrain, which accounts for these lattice effects, signifies a decrease from  $3.38 \times 10^{-3}$  to  $1.94 \times 10^{-3}$  due to the presence of AuNPs. This decrease indicates that the lattice distortions within the material are less pronounced or mitigated when AuNPs are incorporated into the structure.

### 3.2. SEM analysis

SEM images of Au NP thin films deposited by 26 mJ and 36 mJ laser pulse energies are given in Fig. 3a and b. While the particles grown on the substrate with low laser pulse energies were small and low in density, the particles produced with large size and high density were realized by high laser pulse energies. So, since fewer Au atoms are ablated with low laser energies, the plasma volume formed by these atoms is tiny, as seen in the inset of Fig. 3a. In addition, the kinetic energy of the ablated atoms is low. Therefore, since the density and points of atoms coming on the substrate are low, the nucleation and particles formed by these atoms are small in size, and the particle density is low. However, it is found to be more significant in the higher energetic and dense plasma of Au atoms formed by higher-laser pulse energies, shown as an inset of Fig. 3b. The highly energetic Au particles attributed to the AuNPs clusters are in Fig. 3b.<sup>34</sup>

CZTS(1) thin films are formed from particles of 250 nm size in Fig. 4a. As the deposition rate increases, particle aggregation and growth improve, the particles constructing CZTS(2) thin film are more significant.<sup>35</sup> CZTS(2) constituted from about 400 nm sized particles, as shown in Fig. 4c. AuNPs ablated by 36 mJ laser pulse energy were embedded into CZTS(1) and CZTS(2) thin films. Embedding AuNPs into CZTS thin films causes the particle agglomeration to grow and the particle size to increase, as stated above. Therefore, the size of particles making up AuNPs@CZTS thin films is comparable to the non-embedded CZTS thin films. In Fig. 4b and d, it can be seen that the particle size of AuNPs@CZTS(1) & (2) thin films increased pronouncedly.<sup>1,36,37</sup>

### 3.3. SEM-EDX analyses

Fig. 5 and Table 2 show that AuNPs@CZTS thin films are rich in Sn because the 375 °C annealing temperature is not very high.

Table 1 Grain size, dislocation density, microstrain, and crystalline number of CZTS and AuNPs@CZTS thin films

Samples	Grain size (nm)	Dislocation density $\times 10^{16}$ (lines per $\text{m}^2$ )	Micro-strain $\times 10^{-3}$
CZTS(1)	7.34	1.86	4.93
AuNPs@CZTS(1)	12.1	0.68	2.99
CZTS(2)	10.71	0.72	3.38
AuNPs@CZTS(2)	18.64	0.28	1.94



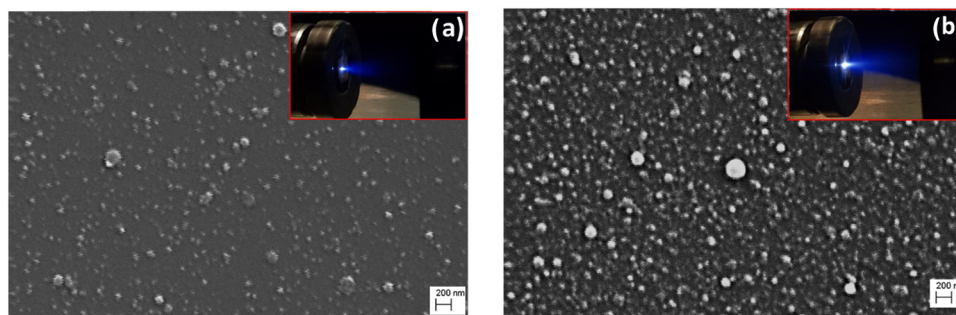


Fig. 3 SEM image of Au nanoparticles (and the plasma photograph of the ablated Au material) of the deposited Au nanoparticles by (a) 26 mJ and (b) 36 mJ laser energy.

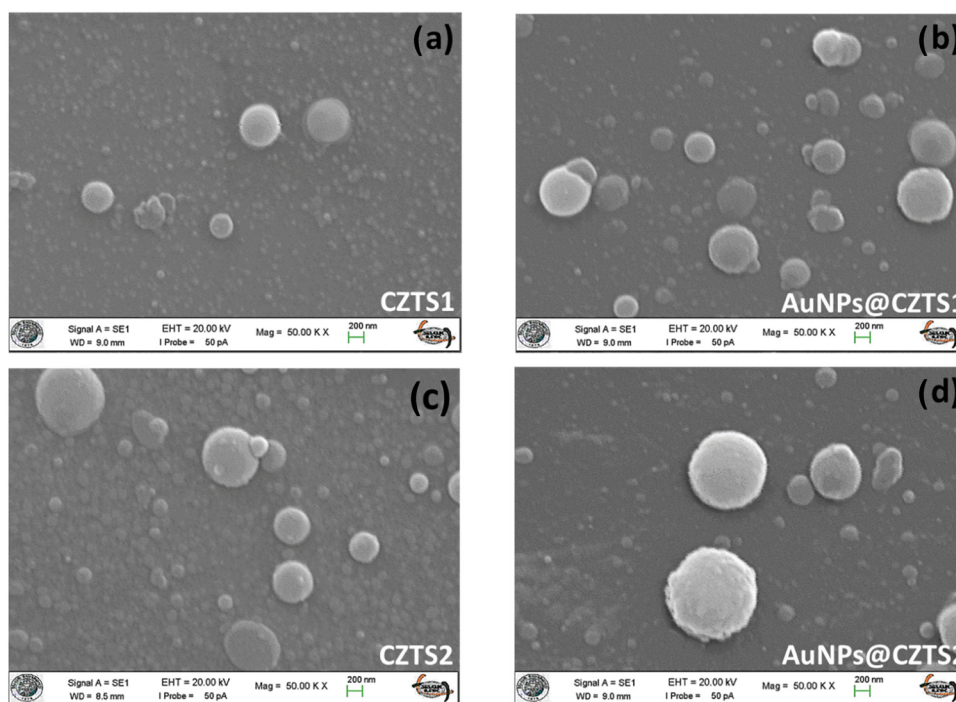


Fig. 4 SEM images of CZTS and AuNPs@CZTS thin films.

However, during the annealing process of thin films, Sn elements tend to evaporate and diffuse towards the film surface, which causes the amount of Sn in a thin film to be excessive on the surface.<sup>38–41</sup> The amount of Cu is higher than that of Zn, indicating that  $\text{Zn}^{2+}$  ions have replaced  $\text{Au}^{3+}$  ions. Increasing the thickness of thin films led to some decrease in Sn and a more ideal stoichiometric transfer.  $\text{Cu}_{\text{Zn}}$  acceptor defects can occur in AuNPs@CZTS(2), a thin film that enhances its p-type feature.<sup>42</sup> Furthermore, the Zn/Sn ratio increase indicates that AuNPs@CZTS(2) thin film turns into an ideal stoichiometric structure.

### 3.4. Optical analyses

The absorption spectrum of AuNPs ablated by the laser beam with energies in the 26 mJ and 36 mJ range and then deposited on substrates is given in Fig. 6. The deposited AuNPs have

exhibited LSPR properties. The LSPR peak shifted towards the more extended wavelength region in the solar spectrum while the laser beam energy increased. So, the density of ablated particles deposited on the substrate shows some increment with some increase in laser energies. The near-field interaction between AuNPs and larger particle sizes causes the redshift. LSPR peaks of particles deposited using 36 mJ, 32 mJ, 30 mJ, and 26 mJ laser energies appeared at 820 nm, 725 nm, 686 nm, and 648 nm positions in the spectrum, respectively.<sup>43</sup> The particles deposited using 26 mJ laser pulse energy have a low density and a small particle size. Electrons in the particle are excited by the EMF of the radiation, making simultaneous oscillating motion and providing the damping of the electric field of the light by the dipole field.<sup>44–46</sup> The large particle size and the near-field interaction between the particles can result in some distortion of the oscillation by affecting the restoring



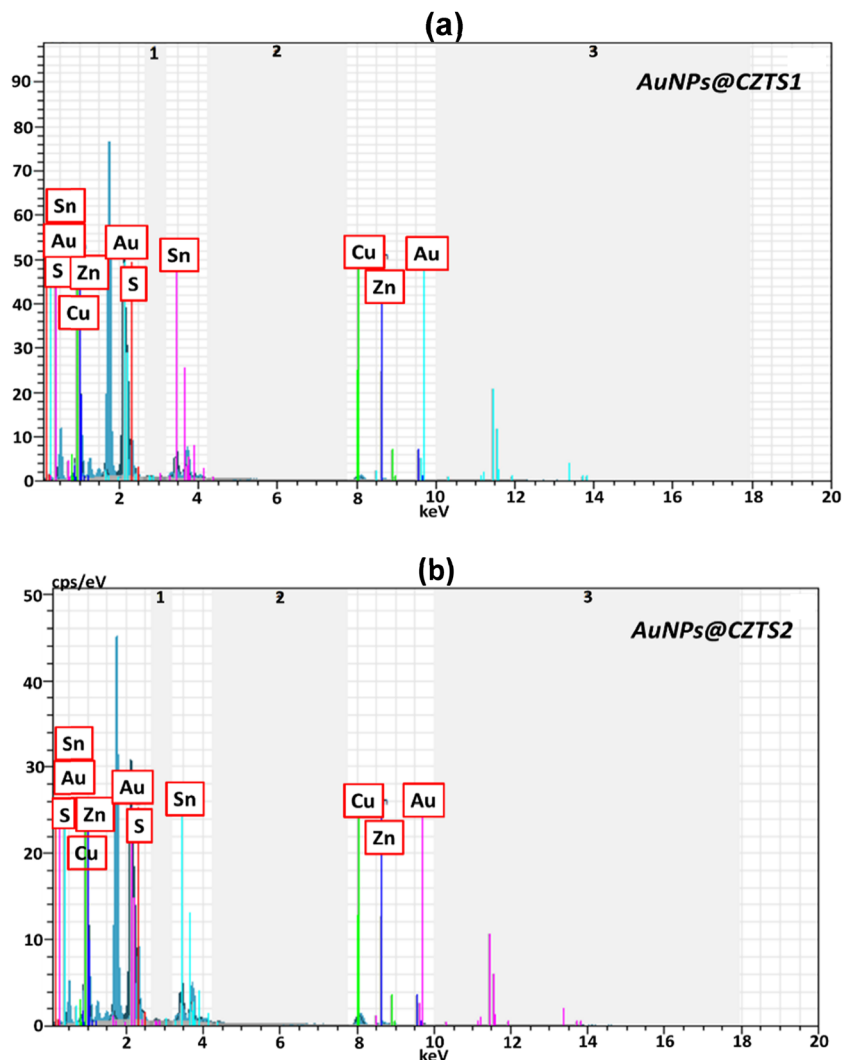


Fig. 5 SEM-EDX spectra of (a) AuNPs@CZTS(1) and (b) AuNPs@CZTS(2) thin films.

Table 2 Atomic weights of elements constituting AuNPs@CZTS(1) and AuNPs@CZTS(2) thin films

Thin films	Cu (%)	Au (%)	Zn (%)	Sn (%)	S (%)
AuNPs@CZTS(1)	24.03	6.66	8.78	27.34	33.18
AuNPs@CZTS(2)	27.33	6.32	8.32	20.14	37.89

force that causes the movement of electrons in the particle, leading to the LSPR peak shifting towards the more extended wavelength region.

Depending on the LSPR peak wavelength, the size of NP forming the Au thin film can be calculated by eqn (4):

$$d = \frac{\ln\left(\frac{\lambda_{\text{LSPR}} - \lambda_0}{L_1}\right)}{L_2} \quad (4)$$

where  $\lambda_0 = 530$  nm is the primary LSPR wavelength for Au nanoparticles;  $L_1 = 6.53$  and  $L_2 = 0.0212$ , are constants and  $\lambda_{\text{LSPR}}$

is the LSPR wavelength of thin films produced.<sup>47</sup> NPs forming Au thin films were calculated to be 175 nm, 157 nm, 146 nm,

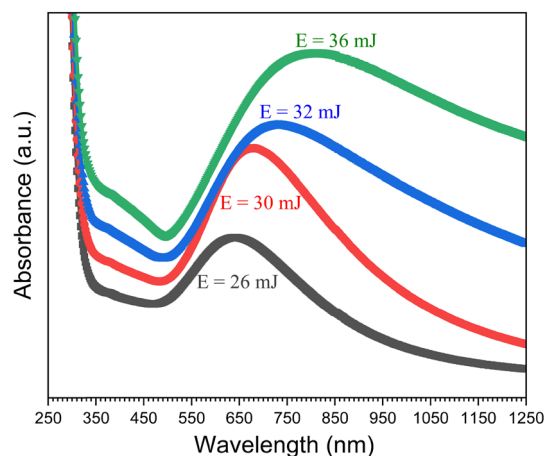


Fig. 6 The absorption spectra of Au plasmonic nanoparticles depending on laser pulse energy.



and 133 nm for LSPR peaks that appeared at 820 nm, 725 nm, 686 nm, and 648 nm wavelengths, respectively. As stated above, some increases in the LSPR peak confirmed the increase in the particle size.

In the absorption spectrum presented in Fig. 7a, it is observed that the CZTS(1) thin film without embedded AuNPs exhibits a lower absorption intensity in the near-infrared (NIR) and visible (Vis) regions compared to the AuNPs@CZTS(1) sample. AuNPs@CZTS(1) demonstrates an enhanced absorption capacity, notably presenting a localized surface plasmon resonance (LSPR) peak at a wavelength of 763 nm, attributable to the plasmonic properties of the embedded gold nanoparticles (AuNPs). This enhancement in absorption intensity in the Vis and NIR regions is a direct consequence of the presence of AuNPs. Furthermore, the AuNPs@CZTS(2) thin film, doped with AuNPs using a 36 mJ laser pulse energy, exhibits even higher absorption intensity in these regions than the CZTS(1) thin film. This difference highlights the significant role of laser energy in modulating the optical properties of the AuNP-doped CZTS films.

The Tauc equation expressed below is used to calculate the band gap of thin films:

$$(\alpha h\nu)^2 = A(h\nu - E_g) \quad (5)$$

$E_g$  is the thin film band gap,  $A$  is a constant, and  $h\nu$  is the photon energy. The extrapolation of the linear line of  $(\alpha h\nu)^2$  versus  $(h\nu)$  in the Tauc plot allows  $E_g$  to be obtained as in Fig. 8. The direct band gaps of CZTS(1), CZTS(2), AuNPs@CZTS(1), and AuNPs@CZTS(2) thin films have been determined to be 1.95 eV, 1.90 eV, 1.85 eV, and 1.52 eV, respectively. It has been noticed that the absorption of thin films increases with the doping of AuNPs while their band gap decreases.<sup>48</sup> In addition, Au atoms can lead to some decreases in the band gap as they can form shallow defects in the band gap. Therefore, more photo-excited charge carriers can be included inside thin films with a lower band gap.

The refractive index of CZTS and AuNPs@CZTS semiconductors is a parameter that significantly affects the optical properties of thin films. Different models for calculating the

refractive index were reported in this section. The Moss relation, expressed by eqn (6), was used to calculate the refractive index of a thin film:<sup>49</sup>

$$E_g n^4 = k \quad (6)$$

where,  $k$  is a constant = 108 eV. In addition, the Herve-Vandamme<sup>50</sup> relation indicates the relation between  $E_g$  and  $n$ .

$$n = \sqrt{1 + \left(\frac{X}{E_g + Y}\right)^2} \quad (7)$$

here,  $X$  and  $Y$  are constants with values of 13.6 eV and 3.4 eV, respectively. Furthermore, Ravindra also interestingly revealed the relationship between  $n$  and  $E_g$ , using eqn (8).<sup>16</sup>

$$n = 4.16 - 0.85E_g \quad (8)$$

Moss' and Herve-Vandamme's relations indicate very compatible results with each other. However, although Ravindra's relations are consistent, their values are somewhat small compared to those obtained from the other relations. This can be attributed to the coefficient and multiplier values used in the equations. Nevertheless, the increase in the photon absorption and decrease in the band gap with the embedding of AuNPs caused an increase in the refractive index of CZTS thin films. Therefore, CZTS(1), exhibiting the highest photon transmission, has a low refractive index, while AuNPs@CZTS(2), a thin film with the highest photon absorbance, indicates a high refractive index.

The electric field between the charge carriers in the semiconductor represents the dielectric constant and determines the mobility and density of the charges. Therefore, the dielectric coefficient acting on the photoexcited charge carriers in the photodetector is a factor in determining the performance of the photodetectors. The static dielectric constant ( $\epsilon_0$ ) and the high-frequency dielectric constant ( $\epsilon_\infty$ ) are expressed by eqn (9) and (10):<sup>16</sup>

$$\epsilon_0 = 18.52 - 3.08E_g \quad (9)$$

$$\epsilon_\infty = n^2 \quad (10)$$

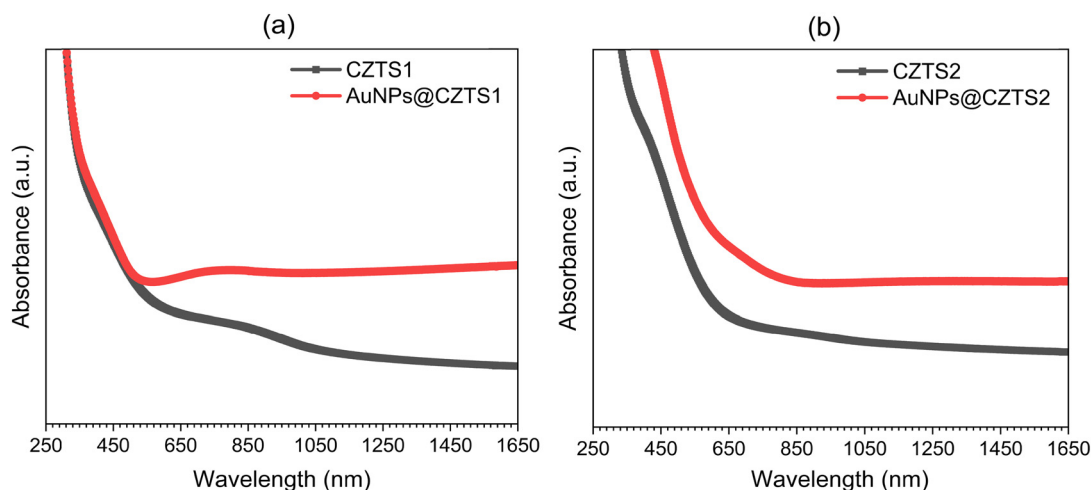


Fig. 7 The absorption spectra of (a) CZTS(1) & (2) and (b) AuNPs@CZTS(1) & (2) thin films.



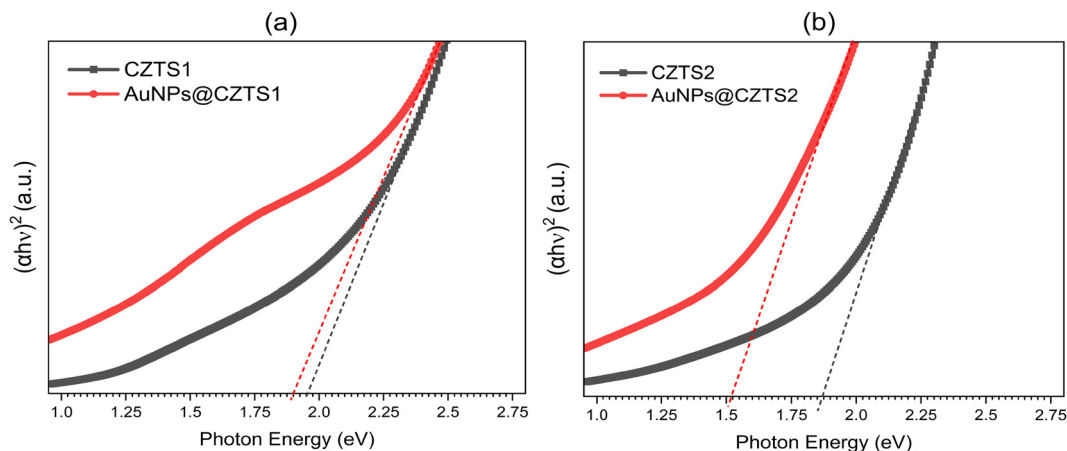


Fig. 8 The Tauc plot of (a) CZTS(1) & (2) and (b) AuNPs@CZTS(1) & (2) thin films.

As seen in Table 3, AuNPs enhance the dielectric coefficients of CZTS thin films. The high dielectric coefficient facilitates the transfer of charges and mobility in the thin films, increases the lifetime of thin films, and therefore provides better responsiveness and high performance of the photodetectors. The dielectric coefficient of the weakest crystalline CZTS(1) thin film is the lowest, while that of the most advanced crystalline AuNPs@CZTS(2) thin film is the highest. Therefore, the recommendation to consider the values from Moss, Herve-Vandamme models more seriously stems from their closer alignment and higher consistency with each other, potentially indicating a more reliable prediction or closer approximation to the actual physical properties being measured. However, assessing the models in the context of specific experimental conditions or theoretical frameworks is essential to ensure the most accurate interpretation.

### 3.5. Photodetector characterization

The photodetection capabilities of nanostructured CZTS and AuNPs@CZTS films were studied by analyzing their dark and 1 Sun illumination current–voltage ( $I$ – $V$ ) characteristics. The  $I$ – $V$  behavior of CZTS and AuNPs@CZTS thin film-based photodetectors was recorded under dark and illuminated conditions over a voltage range from  $-5$  to  $+5$  volts, as shown in Fig. 9(a–d). Notably, all the films demonstrated impressive light detection capabilities under 1 Sun illumination.

In the dark current measurements, the recorded currents ( $I_d$ ) at a bias voltage of 5 V were found to be approximately 2.24 mA, 2.52 mA, 2.65 mA, and 3.33 mA for CZTS(1), CZTS(2), AuNPs@CZTS(1), and AuNPs@CZTS(2) films, respectively

Table 3 Refractive index ( $n$ ), high-frequency dielectric constant ( $\epsilon_\infty$ ) and static dielectric constant ( $\epsilon_0$ ) of CZTS and AuNPs@CZTS thin films

Samples	$E_g$ (eV)	Moss		Herve-Vandamme		Ravindra		
		$n$	$\epsilon_\infty$	$n$	$\epsilon_\infty$	$n$	$\epsilon_\infty$	$\epsilon_0$
CZTS(1)	1.95	2.72	7.44	2.73	7.46	2.50	6.26	12.51
AuNPs@CZTS(1)	1.90	2.74	7.53	2.75	7.58	2.54	6.47	12.66
CZTS(2)	1.85	2.76	7.64	2.77	7.71	2.58	6.69	12.82
AuNPs@CZTS(2)	1.52	2.90	8.42	2.93	8.64	2.86	8.22	13.83

(see Fig. A1, ESI†). These values provide insights into the conductivity of thin films without illumination. The variation in dark currents can be attributed to the thickness of nanostructures and the integration of AuNPs in the CZTS matrix. Notably, the AuNPs@CZTS(2) film demonstrated the highest dark current among all the samples, suggesting its potential for enhanced charge carrier transport and sensitivity, essential for efficient photodetection applications.

This study aims to investigate the time-dependent photoresponse of photodetector CZTS devices. These devices were subjected to intense 1 Sun light pulses with an irradiance of  $100 \text{ mW cm}^{-2}$  to analyze their temporal behavior (Fig. 10a). The measurements were carefully conducted at a fixed bias voltage of 5.0 V. The resulting data are presented in Fig. 10b. Among the CZTS structures integrated with AuNPs, AuNPs@CZTS(2) film emerged as the most efficient device. The one-cycle time-dependent photoresponse of AuNPs@CZTS(2) film is illustrated in Fig. 10c.

The rise and decay times of CZTS and AuNPs@CZTS PDs of 61 and 112 nm CZTS layers in thickness at 5 V are illustrated in Fig. 10d.  $\tau_R$  rise (response) time holds significant importance in photodetectors as it signifies the duration required for the device to detect variations in light intensity and generate an output signal.  $\tau_R$  is particularly critical in applications that demand swift detection and response, such as optical communication systems and high-speed imaging. A shorter  $\tau_R$  enables the photodetector to respond rapidly to changes in light intensity, facilitating faster and more accurate measurements. Conversely, the decay  $\tau_D$  (recovery) time denotes the period required for the photodetector to return to its original state after exposure to a light signal. Phononic scattering pertains to the interaction between charge carriers and lattice vibrations and can affect carrier mobility and, hence, the photodetector speed. If the CZTS2 structure, due to its increased thickness or differences in grain size, presents altered phonon scattering dynamics, this could lead to a more favorable environment for carrier transport. Conversely, increased phononic scattering in CZTS2 could be responsible for its slower response. In addition, the incorporation of AuNPs has a substantial effect



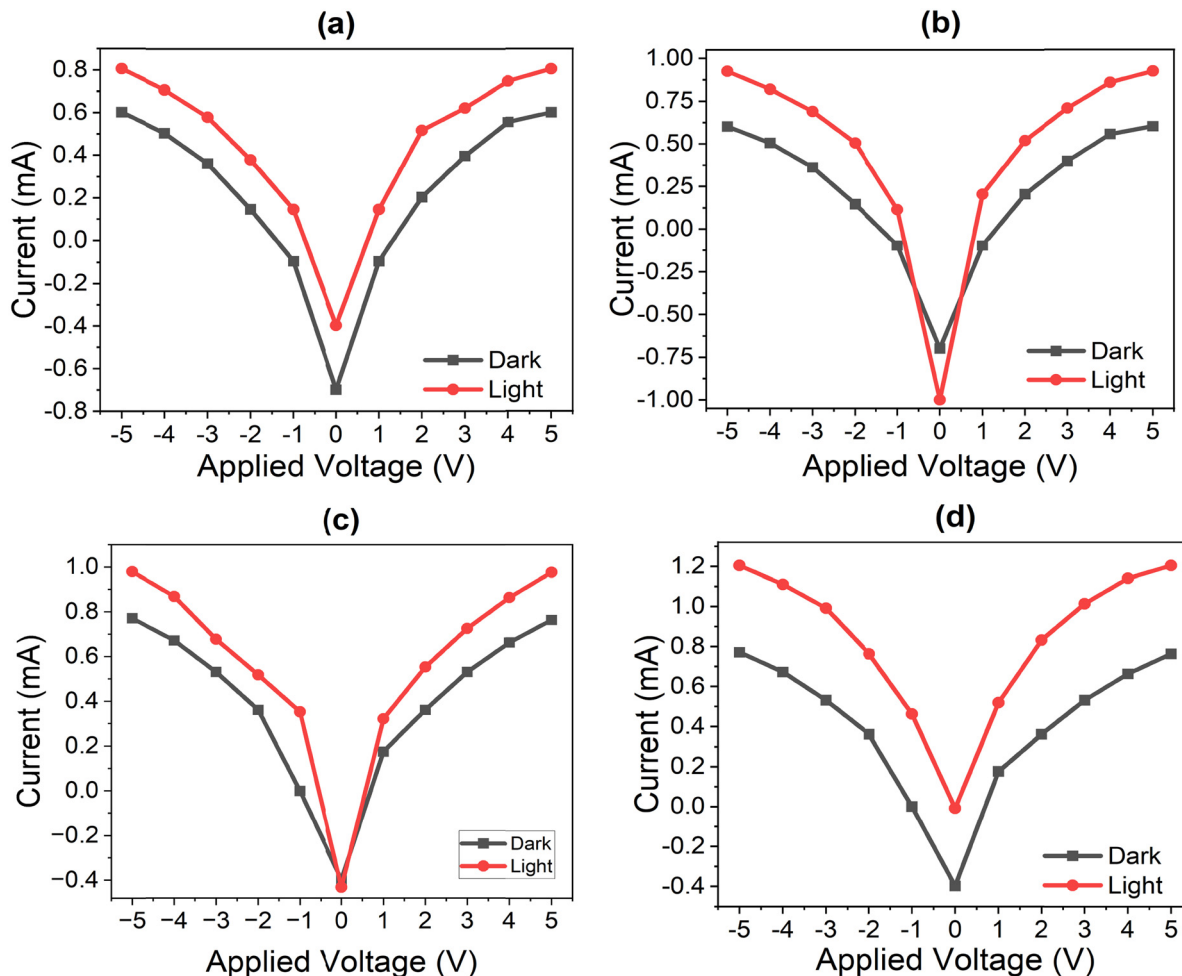


Fig. 9  $I$ - $V$  behavior (a) CZTS(1), (b) CZTS(2), (c) AuNPs@CZTS(1) and (d) AuNPs@CZTS(2) thin films.

on reducing,  $\tau_R$  and  $\tau_D$ , especially in the case of the thicker CZTS film (CZTS(2)). Consequently, the AuNPs@CZTS(2) sample exhibits faster rise ( $\tau_R = 95.4$  ms) and decay ( $\tau_D = 98$  ms) times, aligning with the expected outcomes. The plasmons in AuNPs are excited and form dipoles and the dipoles create an electric field around AuNPs. This way, photoexcited electron and hole pairs occur where the electric field enhancement between AuNPs is close. In particular, photoexcited electrons increase the number and lifetime of minority charge carriers and improve the performance of the photodetector.<sup>16,43,51,52</sup> The LSPR effect is more pronounced in the thicker CZTS2 layer, where the presence of AuNPs effectively mitigates the negative impact of increased layer thickness on the carrier transport.

The photodetector parameters such as responsivity ( $R$ ), detectivity ( $D^*$ ), external quantum efficiency (EQE), and photocurrent gain ( $G$ ) play a crucial role in understanding the influence of the CZTS layer thickness and the incorporation of AuNPs into the CZTS layer. These parameters were calculated using the following expressions eqn (11–14):

$$R = \frac{I_{\text{ph}}}{P \times S} \quad (11)$$

$$D^* = R \sqrt{\frac{S}{2eI_d}} \quad (12)$$

$$\text{EQE} = R \frac{hc}{e\lambda} \quad (13)$$

$$G = \frac{I_{\text{ph}}(I_{\text{ON}})}{I_d(I_{\text{OFF}})} \quad (14)$$

In these equations,  $P$  represents the power of the light source,  $S$  denotes the active area of the device, and  $e$  represents the electronic charge. The results of these parameters were obtained under a bias voltage of 5.0 V and are presented in Fig. 10e.

The investigated parameters exhibited an increasing trend as the CZTS layer thickness increased. The impact of AuNPs on these parameters was found to increase the performance of the device. Consequently, the AuNPs@CZTS(2) configuration demonstrated the highest values across all the studied parameters, including a responsivity of  $0.024 \text{ A W}^{-1}$ , a detectivity of  $6.7 \times 10^8$  Jones, an EQE of 0.35% and a photocurrent gain of 2.8. The performance parameters presented in Fig. 10e – which



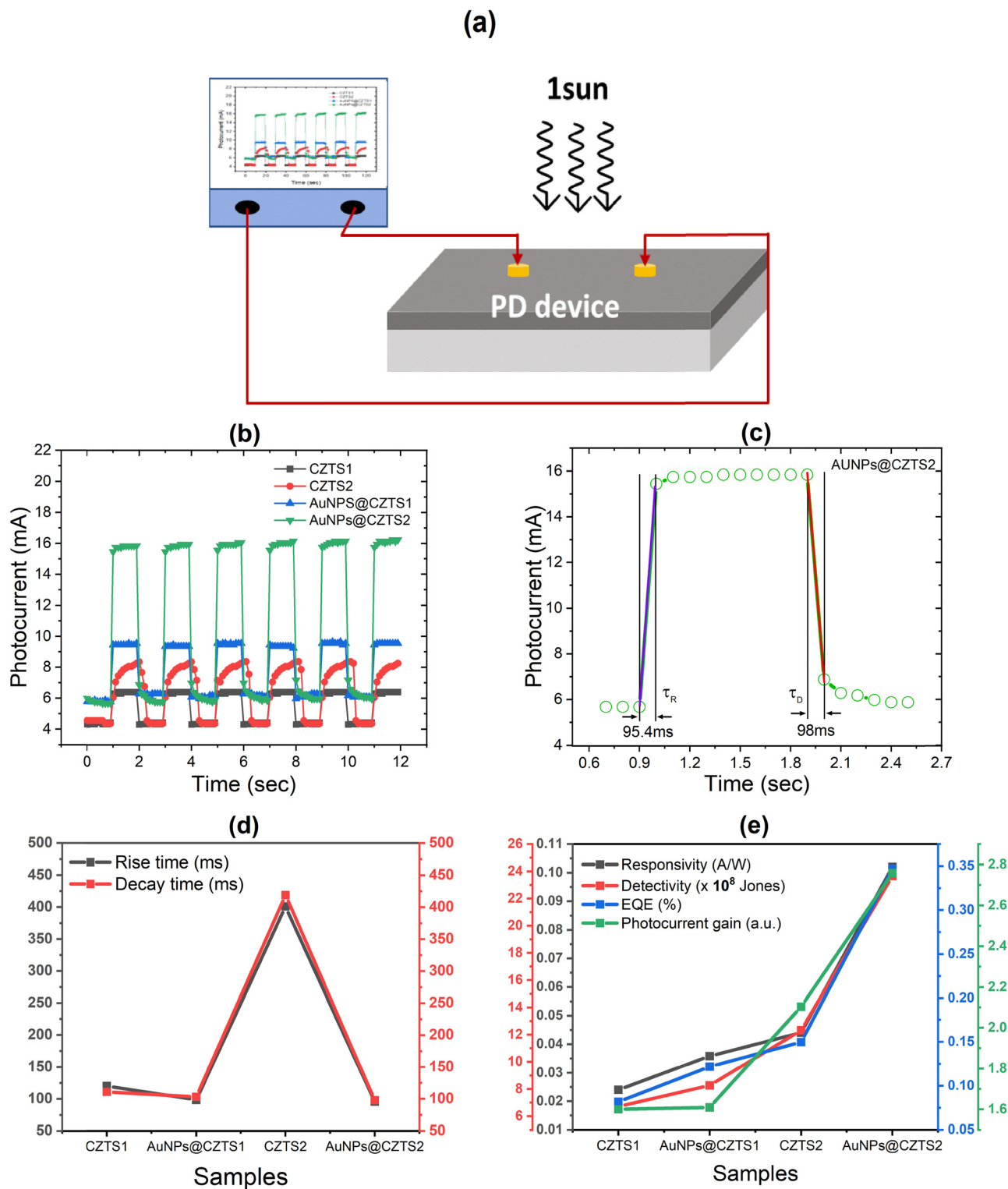


**Fig. 10** Photo-switching characteristics of CZTS-based devices. (a) Schematic illustration of the measurement configuration for photoresponse speed measurement. (b) Time-resolved photoresponse at the bias voltage of 5 V under 1 Sun light illumination. (c) A magnified plot of one response cycle of AuNPs@CZTS(2) in (b) was used to obtain the response and recovery times. CZTS-based devices (d) rise and decay times (e) responsivity, detectivity, EQE, and photocurrent gain.

include responsivity, detectivity, external quantum efficiency (EQE), and photocurrent gain – all show an improvement as the bandgap narrows (see Fig. A2, ESI†). CZTS2, with a lower

bandgap than CZTS1, exhibits a better performance, demonstrating the direct impact of bandgap engineering on the device efficacy. The reduction in the bandgap allows for more efficient



Table 4 Comparison of device performance: current device vs. previous studies on CZTS thin film-based photodetectors

Device	Spectral range (nm)	$R$ ( $A W^{-1}$ )	$D^*$ (Jones)	$\tau_R$ (ms)	$\tau_D$ (ms)	Ref.
AuNPs@CZTS thin film	1 Sun	0.024	$6.70 \times 10^8$	95.4	98	This work
Na-doped CZTS thin film	1064	63	—	1.06	29.8	53
CZTS-Au nanocomposite	450–460	—	—	22400	391 800	54
CZTSSe thin film	532	0.0146	$3.5 \times 10^9$	330	0.986	55
CZTS thin film	1000–1100	13	—	130	700	56
CZTS rice-like	1064	—	$4.48 \times 10^8$	208	175	57
Au/CZTS/FTO	750	0.5	$10^{16}$	—	—	58
CZTS thin film	480	2.02	$15.1 \times 10^8$	3700	4100	59

absorption of the 1 Sun solar spectrum, thus increasing the generation of charge carriers under illumination. This is particularly relevant for photodetectors, where a smaller bandgap can significantly improve the absorption of low-energy photons, which constitute a substantial portion of the solar spectrum.

Previous studies have highlighted the importance of developing cost-effective and uniformly deposited CZTS thin films to enhance the performance of photodetector devices. A comprehensive examination of the existing literature on photodetector devices based on CZTS materials is presented in Table 4. However, this study proposes a novel approach to address these challenges using a simple PLD system.<sup>19</sup> This method enables the fabrication of CZTS thin films with an incorporated plasmonic layer of AuNPs. Consequently, this approach holds significant potential for enhancing the overall performance of PD devices.

## Conclusions

Thin films, CZTS(1) and CZTS(2), with thicknesses of 61 nm and 112 nm, were deposited on soda lime glass utilizing a PLD system, accompanied by the incorporation of Au plasmonic nanoparticles (NPs). This integration notably augmented the grain size within the thin films while enhancing the crystal structure of CZTS(2) films. Notably, the wavelength of the localized surface plasmon resonance peak of AuNPs exhibited a shift from 648 nm to 820 nm in response to increased laser energy. The introduction of LSPR, coupled with the presence of AuNPs, significantly enhanced the NIR photon absorption capabilities of both CZTS(1) and CZTS(2) thin films. This effect resulted in a reduction of their band gaps. The calculated refractive indices, employing Moss, Herve-Vandamme, and Ravindra models, exhibited coherent values. The thin films displayed heightened diffraction indices and dielectric coefficients as the band gaps decreased. Among the fabricated photodetectors, those incorporating 112 nm-thick thin films with AuNPs (AuNPs@CZTS(2)) demonstrated superior performance, displaying the rise and decay times of  $\tau_R = 95.4$  ms and  $\tau_D = 98$  ms, respectively.

## Conflicts of interest

The authors have no relevant financial or non-financial interests to disclose.

## Acknowledgements

The authors are thankful to the Selçuk University's Scientific Research Projects (BAP) Coordination Office for their invaluable support, specifically through the projects numbered 15201070, 19401140, 21406007, and 22401108. Also, thanks to the Selçuk University's High Technology Research and Application Center (İL-TEK) and SULTAN Center for their crucial infrastructural support. The authors also acknowledge Necmettin Erbakan University's Science and Technology Research and Application Center (BITAM) for their contributions.

## References

- S. Y. Gezgin, A. Houimi and H. Ş. Kılıç, Production and photovoltaic characterisation of n-Si/p-CZTS heterojunction solar cells based on a CZTS ultrathin active layers, *Optik*, 2019, **199**, 163370.
- S. Y. Gezgin and H. Ş. Kılıç, The electrical characteristics of ITO/CZTS/ZnO/Al and ITO/ZnO/CZTS/Al heterojunction diodes, *Optik*, 2019, **182**, 356–371.
- S. Yiğit Gezgin and H. Ş. Kılıç, Determination of electrical parameters of ITO/CZTS/CdS/Ag and ITO/CdS/CZTS/Ag heterojunction diodes in dark and illumination conditions, *Opt. Quantum Electron.*, 2019, **51**, 1–22.
- S. Dursun, *et al.*, Investigation of photocatalytic activity (under visible light) of ultrathin CZTS films produced in different thicknesses by PLD method, *Opt. Quantum Electron.*, 2023, **55**(2), 166.
- A. K. Singh, *et al.*, Impact on structural and optical properties of CZTS thin films with solvents and Ge Incorporation, *Int. J. Photoenergy*, 2021, **2021**, 1–9.
- M. A. García, Surface plasmons in metallic nanoparticles: fundamentals and applications, *J. Phys. D: Appl. Phys.*, 2011, **44**(28), 283001.
- S. Y. Gezgin, *et al.*, Effect of Ar gas pressure on LSPR property of Au nanoparticles: Comparison of experimental and theoretical studies, *Nanomaterials*, 2020, **10**(6), 1071.
- C. Noguez, Surface plasmons on metal nanoparticles: the influence of shape and physical environment, *J. Phys. Chem. C*, 2007, **111**(10), 3806–3819.
- A. Houimi, S. Y. Gezgin and H. Ş. Kılıç, The effect of sodium (Na) doping on the performance of n-Si/Cu<sub>2</sub>SnS<sub>3</sub> heterojunction solar cells deposited by PLD using a homemade target, *Optik*, 2022, **264**, 169364.



- 10 J. Polte, Fundamental growth principles of colloidal metal nanoparticles – a new perspective, *CrystEngComm*, 2015, **17**(36), 6809–6830.
- 11 S. Y. Gezgin, Modelling and investigation of the electrical properties of CIGS/n-Si heterojunction solar cells, *Opt. Mater.*, 2022, **131**, 112738.
- 12 H.-U. Krebs, *et al.*, Pulsed Laser Deposition (PLD) – A Versatile Thin Film Technique, in *Advances in Solid State Physics*, ed. B. Kramer, Springer Berlin Heidelberg: Berlin, Heidelberg, 2003, pp. 505–518.
- 13 A. J. Haider, *et al.*, A comprehensive review on pulsed laser deposition technique to effective nanostructure production: trends and challenges, *Opt. Quantum Electron.*, 2022, **54**, 8.
- 14 N. A. Shepelin, *et al.*, A practical guide to pulsed laser deposition, *Chem. Soc. Rev.*, 2023, **52**(7), 2294–2321.
- 15 A. A. Akande, B. N. Masina and B. Mwakikunga, Effect of laser wavelength in PLD in the orientation and thermochromic properties of VO<sub>2</sub>(M<sub>1</sub>) on a glass substrate, *MRS Adv.*, 2020, **5**(21–22), 1121–1132.
- 16 S. Yiğit Gezgin and H. Ş. Kiliç, The effect of Ag plasmonic nanoparticles on the efficiency of CZTS solar cell: an experimental investigation and numerical modelling, *Indian J. Phys.*, 2023, **97**(3), 779–796.
- 17 Ü. Akın, *et al.*, The electrical properties of ZnO/Si heterojunction diode depending on thin film thickness, *J. Korean Phys. Soc.*, 2022, **81**(2), 139–149.
- 18 S. Y. Gezgin, *et al.*, Determination of photovoltaic parameters of CIGS heterojunction solar cells produced by PLD technique, using SCAPS simulation program, *Vacuum*, 2021, **192**, 110451.
- 19 M. A. Basyooni, *et al.*, Observation of negative photoreponse in Joule-heated Au/Cu<sub>2</sub>ZnSnS<sub>4</sub> ternary chalcogenide thin film deposited by low energy pulsed laser deposition, *Opt. Mater.*, 2022, **128**, 112389.
- 20 A. Katerski, *et al.*, Modification of light absorption in thin CuInS<sub>2</sub> films by sprayed Au nanoparticles, *Nanoscale Res. Lett.*, 2014, **9**, 1–6.
- 21 B. K. Patra, *et al.*, Coincident site epitaxy at the junction of Au–Cu<sub>2</sub>ZnSnS<sub>4</sub> heteronanostructures, *Chem. Mater.*, 2015, **27**(3), 650–657.
- 22 S.-N. Park, *et al.*, Solution-processed Cu<sub>2</sub>ZnSnS<sub>4</sub> absorbers prepared by appropriate inclusion and removal of thiourea for thin film solar cells, *RSC Adv.*, 2014, **4**(18), 9118–9125.
- 23 S. Singh, *et al.*, Superior heterojunction properties of solution processed copper-zinc-tin-sulphide quantum dots on Si, *Nanotechnology*, 2017, **28**(43), 435704.
- 24 J. P. Liu, *et al.*, Fabrication and characterization of kesterite Cu<sub>2</sub>ZnSnS<sub>4</sub> thin films deposited by electrostatic spray assisted vapour deposition method, *Phys. Status Solidi A*, 2015, **212**(1), 135–139.
- 25 S. R. Kodigala, *Thin film solar cells from earth abundant materials: growth and characterization of Cu<sub>2</sub>(ZnSn)(SSe)<sub>4</sub> thin films and their solar cells*, Newnes, 2013.
- 26 M. Y. Yeh, *et al.*, Copper-Zinc-Tin-Sulfur Thin Film Using Spin-Coating Technology, *Materials*, 2016, **9**(7), 526.
- 27 W. Bao and M. Ichimura, Influence of secondary phases in kesterite-Cu<sub>2</sub>ZnSnS<sub>4</sub> absorber material based on the first principles calculation, *Int. J. Photoenergy*, 2015, **2015**, 592079.
- 28 D. M. Berg, *et al.*, Discrimination and detection limits of secondary phases in Cu<sub>2</sub>ZnSnS<sub>4</sub> using X-ray diffraction and Raman spectroscopy, *Thin Solid Films*, 2014, **569**, 113–123.
- 29 H. Hussein and A. Yazdani, Doping the bismuth into the host's Cu<sub>2</sub>ZnSnS<sub>4</sub> semiconductor as a novel material for thin film solar cell, *Results Phys.*, 2019, **12**, 1586–1595.
- 30 H. Hussein and A. Yazdani, Investigation the influence of Fe (III) doping in Cu<sub>2</sub>ZnSnS<sub>4</sub> semiconductor: Structural, optical and magnetic properties, *Optik*, 2019, **179**, 505–513.
- 31 D. S. Dhawale, A. Ali and A. C. Lokhande, Impact of various dopant elements on the properties of kesterite compounds for solar cell applications: a status review, *Sustainable Energy Fuels*, 2019, **3**(6), 1365–1383.
- 32 N. Khoshsirar, *et al.*, Efficiency enhancement of Cu<sub>2</sub>ZnSnS<sub>4</sub> thin film solar cells by chromium doping, *Sol. Energy Mater. Sol. Cells*, 2019, **201**, 110057.
- 33 D.-H. Kuo and M. Tsega, Characterizations of Ga-Doped Cu<sub>1.75</sub>Zn(Sn<sub>1-x</sub>Ga<sub>x</sub>)Se<sub>4</sub> Bulks, *ECS J. Solid State Sci. Technol.*, 2014, **3**(5), P155.
- 34 P. K. Diwakar, *et al.*, The influence of laser pulse duration and energy on ICP-MS signal intensity, elemental fractionation, and particle size distribution in NIR fs-LA-ICP-MS, *J. Anal. At. Spectrom.*, 2013, **28**(9), 1420–1429.
- 35 Z. Vakulov, *et al.*, Size effects in LiNbO<sub>3</sub> thin films fabricated by pulsed laser deposition, *J. Phys.: Conf. Ser.*, 2018, **1124**, 022032.
- 36 K. Rawat and P. Shishodia, Enhancement of photosensitivity in bismuth doped Cu<sub>2</sub>ZnSnS<sub>4</sub> thin films, *Phys. Status Solidi RRL*, 2016, **10**(12), 890–894.
- 37 S. Thiruvankadam, *et al.*, Effect of Zn/Sn molar ratio on the microstructural and optical properties of Cu<sub>2</sub>Zn<sub>1-x</sub>Sn<sub>x</sub>S<sub>4</sub> thin films prepared by spray pyrolysis technique, *Phys. B*, 2018, **533**, 22–27.
- 38 W. Feng, *et al.*, Influence of annealing temperature on CZTS thin film surface properties, *J. Electron. Mater.*, 2017, **46**, 288–295.
- 39 G. K. Gupta, V. Reddy and A. Dixit, Impact of excess and disordered Sn sites on Cu<sub>2</sub>ZnSnS<sub>4</sub> absorber material and device performance: a 119Sn Mössbauer study, *Mater. Chem. Phys.*, 2019, **225**, 410–416.
- 40 L. Yao, *et al.*, Reactive mechanism of Cu<sub>2</sub>ZnSnSe<sub>4</sub> thin films prepared by reactive annealing of the Cu/Zn metal layer in a SnSex+ se atmosphere, *Crystals*, 2018, **9**(1), 10.
- 41 J. Zhong, *et al.*, Sulfurization induced surface constitution and its correlation to the performance of solution-processed Cu<sub>2</sub>ZnSn(S, Se)<sub>4</sub> solar cells, *Sci. Rep.*, 2014, **4**(1), 1–9.
- 42 C. Bosson, *Understanding Cu<sub>2</sub>ZnSnS<sub>4</sub> as a Photovoltaic Absorber for the Future of Solar Electricity*, Durham University, 2018.
- 43 S. Y. ğt Gezgin and H. Ş. Kiliç, An improvement on the conversion efficiency of Si/CZTS solar cells by LSPR effect of embedded plasmonic Au nanoparticles, *Opt. Mater.*, 2020, **101**, 109760.



- 44 L.-B. Luo, *et al.*, Surface plasmon resonance enhanced highly efficient planar silicon solar cell, *Nano Energy*, 2014, **9**, 112–120.
- 45 S.-C. Chen, *et al.*, In-situ probing plasmonic energy transfer in Cu (In, Ga) Se<sub>2</sub> solar cells by ultrabroadband femtosecond pump-probe spectroscopy, *Sci. Rep.*, 2015, **5**(1), 1–7.
- 46 X. Zhang, *et al.*, Significant broadband photocurrent enhancement by Au-CZTS core-shell nanostructured photocathodes, *Sci. Rep.*, 2016, **6**(1), 1–8.
- 47 İ. Candan, *et al.*, Biosensor Properties Of Plasmonic Silver Nanoparticles Produced By Pld, *Middle East Tech. Univ. J. Pure Appl. Sci.*, 2021, **7**(2), 112–122.
- 48 L. Wang, *et al.*, Plasmonic silver nanosphere enhanced ZnSe nanoribbon/Si heterojunction optoelectronic devices, *Nanotechnology*, 2016, **27**(21), 215202.
- 49 Y. Akaltun, *et al.*, The relationship between refractive index-energy gap and the film thickness effect on the characteristic parameters of CdSe thin films, *Opt. Commun.*, 2011, **284**(9), 2307–2311.
- 50 P. Herve and L. Vandamme, General relation between refractive index and energy gap in semiconductors, *Infrared Phys. Technol.*, 1994, **35**(4), 609–615.
- 51 N. S. Rohizat, *et al.*, Plasmon-enhanced reduced graphene oxide photodetector with monometallic of Au and Ag nanoparticles at VIS–NIR region, *Sci. Rep.*, 2021, **11**(1), 19688.
- 52 L. B. Luo, *et al.*, The effect of plasmonic nanoparticles on the optoelectronic characteristics of CdTe nanowires, *Small*, 2014, **10**(13), 2645–2652.
- 53 O. P. Singh, *et al.*, Fast switching response of Na-doped CZTS photodetector from visible to NIR range, *Sol. Energy Mater. Sol. Cells*, 2016, **157**, 28–34.
- 54 A. Kumar and A. D. Thakur, Improving the optoelectrical properties of Cu<sub>2</sub>ZnSnS<sub>4</sub> using gold and graphene nanofillers, *J. Mater. Sci.: Mater. Electron.*, 2019, **30**(9), 8546–8554.
- 55 K. S. Gour, *et al.*, Enhanced photoresponse of Cu<sub>2</sub>ZnSn(S, Se)<sub>4</sub> based photodetector in visible range, *J. Alloys Compd.*, 2017, **694**, 119–123.
- 56 M. Banavoth, S. Dias and S. B. Krupanidhi, Near-infrared photoactive Cu<sub>2</sub>ZnSnS<sub>4</sub> thin films by co-sputtering, *AIP Adv.*, 2013, **3**, 8.
- 57 K. S. Gour, *et al.*, Nanostructured Cu<sub>2</sub>ZnSnS<sub>4</sub> (CZTS) thin film for self-powered broadband photodetection, *J. Alloys Compd.*, 2018, **735**, 285–290.
- 58 S. Kukreti, *et al.*, Near-infrared photodetector performance of Cu<sub>2</sub>ZnSnS<sub>4</sub> in the metal-semiconductor-metal configuration: Theoretical studies, *Optik*, 2022, **264**, 169385.
- 59 A. B. Hirpara, *et al.*, Photoresponse application of the dip-coated Cu<sub>2</sub>ZnSnS<sub>4</sub> thin film, *Appl. Phys. A: Mater. Sci. Process.*, 2023, **129**(3), 226.

